

Journal of Power Sources

Submitted September 15, 2014

(Accepted) November 24, 2014

**Characterization of mixed titanium-niobium oxide $\text{Ti}_2\text{Nb}_{10}\text{O}_{29}$ annealed in vacuum
as anode material for lithium-ion battery**

Toshiki Takashima, Tomohiro Tojo, Ryoji Inada*, and Yoji Sakurai

Department of Electrical and Electronic Information Engineering,

Toyohashi University of Technology,

1-1 Hibarigaoka, Tempaku-cho, Toyohashi, Aichi 441-8580, Japan.

*Corresponding author

Ryoji Inada, Associate Professor

Postal address: Toyohashi University of Technology, 1-1 Tempaku-cho, Toyohashi,

Aichi 441-8580, Japan

Phone: +81-532-44-6723

Fax: +81-532-44-6757

E-mail address: inada@ee.tut.ac.jp

Abstract

In this paper, the properties of mixed titanium-niobium oxide $\text{Ti}_2\text{Nb}_{10}\text{O}_{29}$ (TNO) annealed in air and vacuum as anode material for lithium-ion battery were investigated. The color of TNO annealed in vacuum (V-TNO) is dark blue while white for TNO annealed in air (A-TNO). Moreover, lattice parameters for V-TNO were confirmed to be slightly larger than those for A-TNO. Introduction of oxygen defect in V-TNO was confirmed by thermogravimetric analysis. X-ray photoelectron spectroscopy analysis also indicated that Ti^{4+} in V-TNO are partially reduced into Ti^{3+} , due to the introduction of oxygen defect in V-TNO. Electronic conductivity at room temperature for uni-axially pressed V-TNO powder is estimated to be around 10^{-6} – 10^{-5} S cm^{-1} , which is more than three digits higher than that for pressed A-TNO powder ($= 10^{-9}$ S cm^{-1}). The enhancement of intrinsic electronic conductivity of TNO greatly contributes for improving the rate performance. At low current density of 0.5 mA cm^{-2} , both A-TNO and V-TNO showed reversible capacity around 250 mAh g^{-1} at potential range from 1.0 to 2.5 V vs. Li/Li^+ , while at higher current density of 10 mA cm^{-2} , V-TNO maintained much higher discharge capacity of 150 mAh g^{-1} than that for TNO ($= 50 \text{ mAh g}^{-1}$).

Keywords: $\text{Ti}_2\text{Nb}_{10}\text{O}_{29}$, Lithium-ion battery, Anode material, Oxygen defect, Electronic conductivity

1. Introduction

Rechargeable lithium-ion batteries (LiB) have been used as power sources for various electronic devices, such as mobile phones and notebook computers. Graphite has been widely used as an anode material for present LiB because of its low cost, acceptable storage capacity ($= 372 \text{ mAh g}^{-1}$) and stable cycling performance. However, the passivating solid electrolyte interphase (SEI) formed on graphite electrode in the initial charging process by the decomposition of organic liquid electrolyte, which consumes a large amount of lithium irreversibly. Moreover, the low Li^+ storage potential of graphite raises safety issues: when charged at high current rate or overcharged, there is possible lithium plating or formation of lithium dendrites and the short circuit of the battery to fire the flammable electrolyte. Safety concern has become the critical issue for large scale applications of LiB, such as hybrid electric vehicles and energy storage system [1–3].

In order to overcome this problem, titanium-based oxides have attracted wide attention because of relatively high redox potential between 1.0 and 2.0 V vs. Li/Li^+ [4–17], which eliminates the possibility of lithium plating during the charging process. Particularly, the zero-strain $\text{Li}_4\text{Ti}_5\text{O}_{12}$ (LTO) with cubic spinel structure was widely investigated as a highly safe anode material for lithium-ion batteries due to its excellent cycle stability and high rate capability [4–10]. However, theoretical Li^+ storage capacity of LTO is limited to 175 mAh g^{-1} . Development of anode materials with similar properties but with high Li^+ storage capacity is strongly desired to further increase energy density of LiB for large scale applications.

Niobium-based oxides with the redox potentials are in the range from 1.0 to 2.0 V vs. Li/Li^+ have been also considered as interesting candidates for anode material of LiB

with high safety [19–35], because it is possible to realize two-electron transfer per niobium by redox couple of $\text{Nb}^{5+}/\text{Nb}^{3+}$, which results into high Li^+ storage capacity. In addition, these oxides are nontoxic and more importantly, their redox potential should avoid possible lithium plating. To date, the electrochemical properties for various niobium-based oxides have been reported including Nb_2O_5 [19–21], LiNbO_3 [22], LiNb_3O_8 [23], $\text{WNb}_{12}\text{O}_{33}$ [24], $\text{Ti}_2\text{Nb}_2\text{O}_9$ [25], TiNb_2O_7 [19, 26–33] and $\text{Ti}_2\text{Nb}_{10}\text{O}_{29}$ [19, 34, 35]. Among these candidates, mixed titanium-niobium oxides TiNb_2O_7 and $\text{Ti}_2\text{Nb}_{10}\text{O}_{29}$ have high theoretical capacity of 380–390 mAh g^{-1} due to $\text{Ti}^{4+/3+}$, $\text{Nb}^{5+/4+}$ and $\text{Nb}^{4+/3+}$ redox couples [19, 26, 34]. TiNb_2O_7 and $\text{Ti}_2\text{Nb}_{10}\text{O}_{29}$ have the monoclinic “shear ReO_3 structure” with the space group of $C2/m$, consisting of MO_6 ($M = \text{Ti}, \text{Nb}$) octahedra sharing edges and corners [19, 26, 35, 37]. At the potential range from 1.0 to 2.5 V vs. Li/Li^+ , they shows the reversible capacity of 250–300 mAh g^{-1} and reasonably good cycle stability. These properties are comparable with titanium-based anode materials such as $\text{TiO}_2(\text{B})$ [11–14], $\text{Li}_2\text{Ti}_3\text{O}_7$ [16], LiTi_2O_4 [17] and $\text{H}_2\text{Ti}_{12}\text{O}_{25}$ [18].

It has been already reported that the rate capability of TiNb_2O_7 was significantly improved by carbon coating [26, 27], reducing the particle size below 100 nm and controlling the particle morphology [29–33]. The former is effective to increase the extrinsic conductivity of active material while the latter plays a role in Li^+ insertion/deinsertion kinetics, by increasing the reaction interface between the active materials and liquid electrolyte and facilitating transport owing to shorter or simpler diffusion paths for Li^+ ions. Compared with TiNb_2O_7 , the reports for electrochemical property of $\text{Ti}_2\text{Nb}_{10}\text{O}_{29}$ are not many at present, and the previous works have been carried out using micron-order $\text{Ti}_2\text{Nb}_{10}\text{O}_{29}$ particles without carbon coating prepared by simple solid state reaction method [34, 35]. The rate capability of $\text{Ti}_2\text{Nb}_{10}\text{O}_{29}$ is

expected to be improved remarkably by introducing nanostructure as well as TiNb_2O_7 , but generally, the fabrication of nanostructured materials is complex and not suitable for mass production for practical use [29–33].

The reforming the intrinsic properties such as electronic conductivity by doping with alien metal ions and/or controlling annealing atmosphere is another effective method to improve the electrochemical properties of active materials. For example, electronic conductivity of $\text{Li}_4\text{Ti}_5\text{O}_{12}$ is greatly enhanced by Ta^{5+} [8], V^{5+} [9], W^{6+} [10] and Mo^{6+} [11] doping into Ti^{4+} site or introduction of oxygen defect by annealing in reducing atmosphere [8, 11]. The enhancement of electronic conductivity of $\text{Li}_4\text{Ti}_5\text{O}_{12}$ by doping several alien metal or introducing oxygen defect is attributed to the partial reduction from Ti^{4+} to Ti^{3+} for charge compensation, and it strongly contributes to the improvement of the rate performance [8–11]. It has been reported that the electronic conductivity of TiNb_2O_7 is greatly enhanced by substituting small amount of Nb^{5+} into Ti^{4+} site, due to the partial reduction from Ti^{4+} to Ti^{3+} for charge compensation. Nb-doped TiNb_2O_7 ($\text{Ti}_{0.9}\text{Nb}_{2.1}\text{O}_7$) shows better electrochemical performance than stoichiometric TiNb_2O_7 [26], which is mainly attributed to the enhanced electronic conductivity. However, the influence of reforming the intrinsic property of $\text{Ti}_2\text{Nb}_{10}\text{O}_{29}$ on its electrochemical performance has not been fully explored.

In this paper, we synthesized $\text{Ti}_2\text{Nb}_{10}\text{O}_{29}$ via simple solid state reaction by annealing the mixture of TiO_2 and Nb_2O_5 in air and vacuum atmosphere, to reform the intrinsic properties. The influence of the annealing atmosphere on the crystal structure, particle morphology, electronic conductivity and electrochemical property was investigated experimentally.

2. Experimental

Samples were synthesized by a conventional solid state reaction method. Stoichiometric amount of anatase TiO_2 (Kojundo Chemical Laboratory Co., Ltd., 99%) and Nb_2O_5 (Kojundo Chemical Laboratory Co., Ltd., 99.9%) were ground and mixed in ethanol by planetary ball-milling (Nagao System, Planet M2-3F) with zirconia balls for 1 h. The mixture was sealed in a vacuum quartz tube with alumina boat and then annealed at 1100°C for 24 h using a tube furnace. For comparison, the sample was also prepared by annealing the same starting materials at 1100°C for 24 h in air.

Crystal structure of both TNO annealed in air (A-TNO) and TNO annealed in vacuum (V-TNO) were evaluated by X-ray diffractometer (MultiFlex, Rigaku) using $\text{CuK}\alpha$ radiation ($\lambda = 0.15418$ nm), with measurement angle range $2\theta = 5\text{--}90^\circ$ and step interval of 0.01° . For the measurements, small amount of Si powders were mixed with A-TNO or V-TNO as the reference material. Using the X-ray diffraction (XRD) data for both powder samples, lattice parameters were calculated by Rigaku PDXL XRD analysis software. Scanning electron microscope (SEM, VE-8800, KEYENCE) was used to observe the size and the morphology of both A-TNO and V-TNO particles. The chemical states of Ti and Nb for both samples were characterized by using an X-ray photoelectron spectrometer (Quantera SXM, ULVAC-PHI Inc.) with an $\text{AlK}\alpha$ X-ray source (1486.6 eV). Thermogravimetric (TG) analysis of both A-TNO and V-TNO was carried out by using differential thermal balance analyzer (Thermo plus EVO II TG-DTA TG8120, RIGAKU) at temperature range from room temperature to 1000°C in flowing air with 500 mL/min, to evaluate the introduction of oxygen defect in V-TNO.

Electronic conductivity for both V-TNO and A-TNO was evaluated at 20°C by potentiostatic polarization measurement with an applied DC voltage of 1 V, using a

multichannel potentiostat (VSP-300, Bio-Logic). During the conductivity measurement, uni-axial pressure of 5×10^3 N was applied to both powder samples put between the pair of SUS316L electrodes with cylindrical shape. For electrochemical characterization of both A-TNO and V-TNO annealed in different atmospheres, two-electrode set-up was used. Firstly, the composite electrodes were fabricated from a 70:25:5 (wt%) mixture of active material (V-TNO or A-TNO), acetylene black (AB) as a conducting additive, and polytetrafluoroethylene (PTFE) as a binder. The mixture was rolled into thin sheet with its thickness of 0.3 mm and punched into 8 mm-diameter circular disks. A-TNO or V-TNO pellet is used as working electrode, where as a single lithium foil serve as both counter and reference electrodes. The electrolyte solution was 1 mol LiPF_6 in a mixture of ethylene carbonate (EC) and dimethyl carbonate (DMC) with a volume ratio of 1:1 (Kishida Chemical Co., Ltd.). Together with Celgard 3501 as a separator, these components were assembled in a CR2032 coin type cell. The assembly of the cell was carried out in a dry Argon-filled glove box (UN-650FCH, UNICO). The cell was charged and discharged over a voltage range between 1.0 and 2.5 V versus Li/Li^+ electrode at different fixed current density 0.5–10 Acm^{-2} and 20°C using Battery Test System (TOSCAT-3100, Toyo System). Electrochemical impedance of the cells with A-TNO and V-TNO electrodes were measured at applied AC voltage amplitude of 10 mV and frequency range of 5– 10^6 Hz, using a Chemical Impedance Meter (3532-80, Hioki). The impedance measurement was carried out on the cell cycled in the voltage 1–2.5 V after 3 charge and discharge for both cells.

3. Results and discussion

Fig. 1(a) and (b) shows the comparison of XRD patterns for A-TNO (annealed in

air) and V-TNO (annealed in vacuum). It is noted that the diffraction peaks from Si, which was mixed with A-TNO or V-TNO as the reference, are removed from the data. All the peaks for both samples are well indexed with the calculated patterns based on structural data for $\text{Ti}_2\text{Nb}_{10}\text{O}_{29}$ with monoclinic ReO_3 shear structure with the space group of $C2/m$ (Fig. 1(c)) [37], and no other peaks from secondary phases were detected. However, as shown in Fig. 1(b), (1 1 0), (0 0 4) and (1 1 -2) peaks are slightly shifted to smaller angle. It is noted that all diffraction peaks for V-TNO are confirmed to be shifted to smaller angle and the angle shift for each diffraction peak is much larger than the measuring step ($= 0.01^\circ$), so that the lattice size for V-TNO is expected to be larger than that for A-TNO. The lattice parameters calculated by using XRD data and PDXL software are $a = 2.053$ nm, $b = 0.3813$ nm, $c = 1.5564$ nm and $\beta = 113.48^\circ$ for A-TNO, while $a = 2.054$ nm, $b = 0.3815$ nm, $c = 1.5575$ nm and $\beta = 113.58^\circ$ for V-TNO. Although these are very close to the data as previously reported [34, 35, 37], the parameters a , b and c for V-TNO are slightly larger than those for A-TNO.

Comparison of photos and SEM images of A-TNO and V-TNO are shown in Figs. 2 and 3, respectively. Both the size and morphology of A-TNO and V-TNO particles are nearly identical and the averaged particle size of both samples is confirmed to be around 1–2 μm . However, as shown in Fig. 2, the color is clearly different among the samples. A-TNO annealed in air is white while V-TNO annealed in vacuum is dark blue. Similar color change was reported in $\text{Li}_4\text{Ti}_5\text{O}_{12}$ with the presence of the mixed $\text{Ti}^{4+}/\text{Ti}^{3+}$ ions for charge compensation by Ta^{5+} [8], V^{5+} [9], W^{6+} [10] and Mo^{6+} [11] doping into Ti^{4+} site. In our experiment, the nominal composition ratios of Ti : Nb of A-TNO and V-TNO are expected to be identical ($= 2 : 10$). Therefore, if partial reduction from Ti^{4+} to Ti^{3+} was occurred in V-TNO annealed in vacuum, some amount of oxygen defect should be

introduced in V-TNO.

In order to confirm the introduction of oxygen defect in V-TNO, thermogravimetric (TG) analysis of both A-TNO and V-TNO was carried out under flowing air. Fig. 4 shows the comparison of thermogravimetric (TG) curves for A-TNO and V-TNO. As can be seen, A-TNO shows no weight change in whole measured temperature range, while the weight of V-TNO begins to increase at temperature above 100°C and becomes constant above 400°C. Increase of the weight for V-TNO from the initial state is confirmed to be 0.5% and after the measurement, the color of V-TNO was changed into white color similar with A-TNO. These results suggest that oxygen defect is introduced in V-TNO and increase of the weight for V-TNO in TG analysis is attributed to the vanishing the oxygen defect by the oxidation. If Ti and Nb contents in V-TNO were stoichiometric (Ti : Nb = 2 : 10), oxygen content in V-TNO is estimated to be 28.53. Therefore, Ti^{4+} and/or Nb^{5+} in V-TNO are expected to be partially reduced into Ti^{3+} and/or Nb^{4+} by introducing oxygen defect. In addition, ionic radii for Ti^{3+} and Nb^{4+} are 67 pm and 68 pm, larger than those for Ti^{4+} (61 pm) and Nb^{5+} (64 pm). Therefore, slightly larger lattice parameters of V-TNO compared with A-TNO as mentioned above could be attributed to the presence of Ti^{3+} and Nb^{4+} .

We carried out X-ray photoelectron spectroscopy (XPS) analysis for both powder samples, to confirm the chemical state of Ti and Nb in A-TNO and V-TNO. The XPS characterizations obtained for both A-TNO and V-TNO powder samples are shown in Fig. 5. As shown in Fig. 5(a), the peak of Ti $2\text{P}_{3/2}$ spectrum in A-TNO is observed at binding energy around 459.2 eV, suggesting that the existence and occupying of Ti^{4+} in an octahedral environment [9–11]. On the other hand, Ti $2\text{P}_{3/2}$ spectra in V-TNO has not only the main peak around 459.0 eV for the presence of Ti^{4+} but also small shoulder

around 457.8 eV. The latter could be attributed to the presence of Ti^{3+} [9–11], caused by introduction of oxygen defect in V-TNO. In Fig. 5(b) for Nb 3d spectra, two peaks located at 207.5 eV for Nb $3d_{5/2}$ and 210.2 eV for Nb $3d_{3/2}$ are confirmed in A-TNO indicating the presence of Nb^{5+} [38, 39]. Although these two peaks are also detected in V-TNO, they are slightly shifted to lower binding energy. Shoulders around 206.6 eV and 209.5 eV, which is attributed to the presence of Nb^{4+} [38, 39], was not confirmed clearly. Therefore, the presence of Nb^{4+} in V-TNO could not be characterized enough.

Potentiostatic polarization measurement at 20°C was carried out to determine the electronic conductivity for A-TNO and V-TNO. Each powder sample was put between the pair of SUS316L electrode with cylindrical shape and then uni-axially pressed under applying pressure of 5×10^3 N. Applied DC voltage in the measurement was fixed to 1.0 V. Geometrical parameter of both pressed powder samples are 12 mm in diameter, 1.2 mm in thickness. The electrical resistance R_e of each pressed powder sample is calculated by dividing the steady state current by applied DC voltage. The electronic conductivity σ_e of pressed powder sample can be derived by using R_e and geometrical parameters as mentioned above. As a result, the electronic conductivity of pressed V-TNO was estimated to be 8×10^{-6} S cm^{-1} , while the conductivity of pressed A-TNO was 5×10^{-9} S cm^{-1} . This indicates that the electronic conductivity of TNO is increased by three digits or more by introduction of oxygen defect, which will drastically influence the rate capability of TNO.

Fig. 6 is the comparison of cell voltage profiles in initial charging (Li^+ insertion) process for A-TNO and V-TNO electrodes at 20°C and current density of 0.5 mA cm^{-2} . As shown in Fig. 6(a), both A-TNO and V-TNO shows narrower voltage plateau around 1.9 V and wider plateau around 1.65 V, which is consistent with the results as previously

reported [34, 35]. It has been considered that in Li^+ insertion process into TNO, the former could be mainly due to the valence variation from Ti^{4+} to Ti^{3+} while latter could be contributed to the reduction from Nb^{5+} to Nb^{4+} , and the reduction from Nb^{4+} to Nb^{3+} could contribute at the potential range below 1.3 V vs Li/Li^+ [34]. It is confirmed that V-TNO electrode shows slightly smaller polarization at cell voltage below 1.65 V and larger specific capacity for Li^+ insertion ($= 252 \text{ mAh g}^{-1}$) than A-TNO ($= 241 \text{ mAh g}^{-1}$). As shown in Fig. 6(b), the capacity at voltage plateau around 1.9 V in V-TNO seems to be smaller than in A-TNO. This is because that the content of Ti^{4+} in V-TNO becomes smaller than A-TNO, due to the introduction of oxygen defect in V-TNO.

The initial charge–discharge curves of both A-TNO and V-TNO electrodes at 20°C and various fixed current densities per unit-electrode area of 0.5, 2, 4 and 7 mA cm^{-2} are shown in Fig. 7. At low current density of 0.5 mA cm^{-2} , both electrodes showed the reversible capacity of 240–250 mAh g^{-1} . The charge and discharge capacities for both electrodes are decreased monotonically with increasing current densities, but V-TNO shows much smaller polarization and larger capacity than A-TNO under the current density above 2 mA cm^{-2} . This tendency becomes more significant as the current density is increased. In Fig. 8, discharge capacities of A-TNO and V-TNO are plotted against discharge current density from 0.5 to 10 mA cm^{-2} . At the highest current density of 10 mA cm^{-2} , V-TNO maintains the discharge capacity of 150 mAh g^{-1} while the capacity of A-TNO is limited to only 50 mAh g^{-1} . Such remarkable improvement of rate performance in V-TNO is mainly attributed to the enhancement of intrinsic electronic conductivity by introduction of oxygen defect.

Fig. 9 shows the cycle stability for both charge and discharge capacity of A-TNO and V-TNO electrodes at 20°C and fixed current density of 2 mA cm^{-2} . As can be seen,

both A-TNO and V-TNO electrodes show reasonably good cycle stability during 30 cycles. Such cycle stability is consistent with the results as previously reported [34, 35]. At same current density, however, V-TNO electrode has much higher specific capacity (= 220–230 mAh g⁻¹) than A-TNO electrode (= 170–180 mAh g⁻¹) due to higher intrinsic electronic conductivity of V-TNO. It is also confirmed that the capacity retention after 30 cycles for both electrodes was around 95%. Moreover, the coulombic efficiency for both electrodes was nearly equal to 100% excepting the first cycle. These results indicate that introduction of oxygen defect in TNO annealed in vacuum has no notable influence on the reversibility of Li⁺ insertion and extraction.

Finally, the Nyquist plots of electrochemical impedance of coin cells with A-TNO and V-TNO electrodes at the cell voltage of 2.3 V are compared in Fig. 10. Before the impedance measurements, each cell was cycled in the voltage 1–2.5 V after 3 charge and discharge. It is confirmed that the Nyquist plots for both electrodes consist of a semicircle with the charge-transfer resistance (R_{ct}) at the electrode-electrolyte interface. The high frequency intercept at the real axis corresponds to the ohmic resistance of the cell mainly contributed from the electrolyte (R_s). Since the frequency range of our experimental set-up is limited above 5 Hz, typical straight line indicating a Warburg impedance due to the diffusion of Li⁺ ions into the electrode could not be observed in the low frequency region. Therefore, the influence of the introduction of oxygen defect on the diffusion of Li⁺ ions in TNO crystal could not be discussed at present and further examination should be necessary in future. However, it is evident that the size of semicircle for V-TNO electrode is much smaller than that for A-TNO, indicating that R_{ct} of V-TNO electrode is much smaller than A-TNO. This is mainly due to the enhanced electronic conductivity for V-TNO particles and the proof for better electrochemical

performance of V-TNO electrode.

4. Conclusion

We prepared $\text{Ti}_2\text{Nb}_{10}\text{O}_{29}$ annealed in air (A-TNO) and vacuum (V-TNO) as the anode material for lithium-ion battery. Although the crystal structure, size and morphology for A-TNO and V-TNO are nearly identical, the color of V-TNO is dark blue while A-TNO is white. Thermogravimetric analysis showed the introduction of oxygen defect in V-TNO annealed in vacuum. XPS analysis also indicated that Ti^{4+} in V-TNO are partially reduced into Ti^{3+} due to the introduction of oxygen defect. Room temperature electronic conductivity for uni-axially pressed V-TNO powder is estimated to be around 10^{-6} – 10^{-5} S cm^{-1} , which is much higher than that for pressed A-TNO powder ($= 10^{-9}$ S cm^{-1}). At low current density of 0.5 mA cm^{-2} , both A-TNO and V-TNO showed reversible capacity of 250 mAh g^{-1} at potential range from 1.0 to 2.5 V vs. Li/Li^+ . At higher current density, however, V-TNO showed much higher capacity than that for A-TNO. The improvement of rate performance in V-TNO is mainly attributed to the enhancement of intrinsic electronic conductivity. These results suggest that V-TNO can potentially be used as novel anode material of high power lithium-ion battery for large scale applications.

Acknowledgements

This work was partly supported by Research Grant from The Hibi Science Foundation and also from The Kazuchika Okura Memorial Foundation.

References

- [1] J.M. Tarascon, M. Armand, *Nature* **414** (2001) 359–367.
- [2] B. Scrosati, J. Garche, *J. Power Sources* **195** (2010) 2419–2430.
- [3] J.B. Goodenough, Y. Kim, *J. Power Sources* **196** (2011) 6688–6694.
- [4] Z. Chen, I. Belharouak, Y.-K. Sun, K. Amine, *Adv. Funct. Mater.* **23** (2013) 959–969.
- [5] T. Ohzuku, A. Ueda, N. Yamamoto, *J. Electrochem. Soc.* **142** (1995) 1431–1435.
- [6] D. Yoshikawa, Y. Kadoma, J.M. Kim, K. Ui, N. Kumagai, N. Kitamura, Y. Idemoto, *Electrochimica Acta* **55** (2010) 1872–1879.
- [7] M-S. Song, A. Benayad, Y-M. Choia, K-S. Park, *Chem. Commun.* **48** (2011) 516–518.
- [8] J. Wolfenstine, J.L. Allen, *J. Power Sources* **180** (2008) 582–585.
- [9] Z. Yu, X. Zhang, G. Yang, J. Liu, J. Wang, R. Wang, J. Zhang, *Electrochimica Acta* **56** (2011) 8611–8617.
- [10] Q. Zhang, C. Zhang, B. Li, D. Jiang, S. Kang, X. Li, Y. Wang, *Electrochimica Acta* **107** (2013) 139–146.
- [11] H. Song, T.G. Jeong, Y.H. Moon¹, H.H. Chun, K.Y. Chung, H.S. Kim, B.W. Cho, Y.T. Kim, *Scientific Report* **4** (2014) 4350.
- [12] M. Inaba, T. Oba, F. Niina, Y. Murota, Y. Ogino, A. Tasaka, K. Hirota, *J. Power Sources* **189** (2009) 580–584.
- [13] Y. Ren, Z. Liu, F. Pourpoint, A. R. Armstrong, C.P. Grey, P.G. Bruce, *Angew. Chem.* **124** (2012) 2206–2209.
- [14] M. Saito, Y. Nakano, M. Takagi, N. Honda, A. Tasaka, M. Inaba, *J. Power Sources*, **244** (2013) 50–55.

- [15] A. Kuhn, R. Amandi, F. Garcia-Alvarado, J. Power Sources **92** (2001) 221–227.
- [16] C. Villevielle, M. Van Thournout, J. Scoyer, C. Tessier, J. Olivier-Fourcade, J.C. Jumas, L. Moncounduit, Electrochimica Acta **55** (2010) 7080–7084.
- [17] E. Setiawati, M. Hayashi, M. Takahashi, T. Shodai, K. Saito, J. Power Sources **196** (2011) 10133–10140.
- [18] J. Akimoto, K. Kataoka, N. Kojima, S. Hayashi, Y. Gotoh, T. Sotokawa, Y. Kumashiro, J. Power Sources, **244** (2013) 679–683.
- [19] R.J. Cava, D.W. Murphy, S.M. Zahurak, J. Electrochem. Soc. **130** (1983) 2345–2451.
- [20] A. Le Viet, M.V. Reddy, R. Joseb, B.V.R. Chowdaria, S. Ramakrishna, Electrochimica Acta **56** (2011) 1518–1528.
- [21] M. Sasidharan, N. Gunawardhana, M. Yoshio, K. Nakashima, Mater. Res. Bull. **47** (2012) 2161–2164.
- [22] V. Pralong, M.A. Reddy, V. Caignaert, S. Malo, O.I. Lebedev, U.V. Varadaraju, B. Raveau, Chem. Mater. **23** (2011) 1915–1922.
- [23] Z. Jian, X. Lu, Z. Fang, Y.S. Hu, J. Zhou, W. Chen, L. Chen, Electrochem. Commun. **13** (2011) 1127–1130.
- [24] D. Saritha, V. Pralong, U.V. Varadaraju, B. Raveau, J. Solid State Chem. **183** (2010) 988–993.
- [25] J.F. Colin, V. Pralong, M. Hervieu, V. Caignaert, B. Raveau, Chem. Mater. **20** (2008) 1534–1540.
- [26] J.T. Han, Y.H. Huang, J.B. Goodenough, Chem. Mater. **23** (2011) 2027–2029.
- [27] J.T. Han, J.B. Goodenough, Chem. Mater. **23** (2011) 3404–3407.
- [28] X. Lu, Z. Jian, Z. Fang, L. Gu, Y.S. Hu, W. Chen, Z. Wang, L. Chen, Energy

- Environ. Sci. **4** (2011) 2638–2644.
- [29] K. Tang, X.K. Mu, P.A. Aken, Y. Yu, J. Maier, *Adv. Energy Mater.* **3** (2012) 49–53.
- [30] L. Fei, Y. Xu, X. Wu, Y. Li, P. Xie, S. Deng, S. Smirnov, H. Luo, *Nanoscale* **5** (2013) 11102–11107.
- [31] C. Jo, Y. Kim, J. Hwang, J. Shim, J. Chun, J. Lee, *Chem. Mater.* **26** (2014) 3508–3514.
- [32] S. Jayaraman, V. Aravindan, P.S. Kumar, W.C. Ling, S. Ramakrishna, S. Madhavi, *ACS Appl. Mater. Interfaces* **6** (2014) 8660–8666.
- [33] B. Guo, X. Yu, X.G. Sun, M. Chi, Z.A. Qiao, J. Liu, Y.S. Hu, X.Q. Yang, J.B. Goodenough, S. Dai, *Energy & Environ. Sci.* **7** (2014) 2220–2226.
- [34] X. Wu, J. Myao, W. Han, Y.S. Yu, D. Chen, J.S. Lee, J. Kim, L. Chen, *Electrochem. Commun.* **25** (2012) 39–42.
- [35] Q. Cheng, J. Liang, Y. Zhu, L. Si, C. Guo, Y. Qian, *J. Mater. Chem. A* **2** (2014) 17258–17262.
- [36] A.D. Wadsley, *Acta Crystallogr.* **14** (1961) 660–664.
- [37] V.K. Trunov, Z.A. Vladimirova, L.M. Kovba, L.M. Komissarova, *Inorg. Mater.* **1** (1965) 1760–1762.
- [38] R. Romero, J. R. Ramos-Barrado, F. Martin, D. Leinen, *Surf. Interface Anal.* **34** (2004) 888–891.
- [39] Z. Weibin, W. Weidong, W. Xueming, C. Xinlu, Y. Dawei, S. Changle, P. Liping, W. Yuying, B. Li, *Surf. Interface Anal.* **45** (2013) 1206–1210.

Figure captions

Fig. 1. X-ray diffraction patterns (a) and enlarged (1 1 0), (0 0 4), and (1 1 -2) peaks (b) for A-TNO annealed in air and V-TNO annealed in vacuum. Calculated diffraction patterns using structural data described in [37] is plotted in (a). The crystal structure of TNO along *ac*-plane based on the structural data in [37] is also shown in (c).

Fig. 2. Photos of as-synthesized A-TNO annealed in air (a) and V-TNO annealed in vacuum (b).

Fig. 3. SEM images of A-TNO annealed in air (a) and V-TNO annealed in vacuum (b).

Fig. 4. Comparison of thermogravimetric (TG) curves for A-TNO and V-TNO. The measurement was carried out in flowing air with 500 mL/min.

Fig. 5. Comparison for Ti 2p (a) and Nb 3d (b) spectrum for A-TNO and V-TNO measured by X-ray photoelectron spectroscopy.

Fig. 6. Comparison of cell voltage profiles in initial charging (Li^+ insertion) process at 20°C and current density of 0.5 mA cm⁻² for A-TNO and V-TNO electrodes (a). Enlarged profiles around higher voltage plateau of 1.9 V (marked by rectangular with dashed black line) is also shown in (b).

Fig. 7. Charge (solid lines) and discharge (dashed lines) curves at 20°C and different

fixed current densities of 0.5, 2, 4 and 7 mA cm⁻² for (a) A-TNO and (b) V-TNO electrodes.

Fig. 8. Comparison of discharge capacities at 20°C for A-TNO and V-TNO electrodes plotted against discharge current densities. Note that the charge current densities were fixed to 0.5 mA cm⁻².

Fig. 9. Cycling performance of both charge and discharge capacities for A-TNO and V-TNO electrodes at a constant current density of 2 mA cm⁻² at 20°C.

Fig. 10. Nyquist plots of electrochemical impedance of the cells including A-TNO and V-TNO electrode. Z' and Z'' represent real and imaginary parts of AC impedance. The measurements were carried out at 27°C and the cell voltages of 2.3 V.

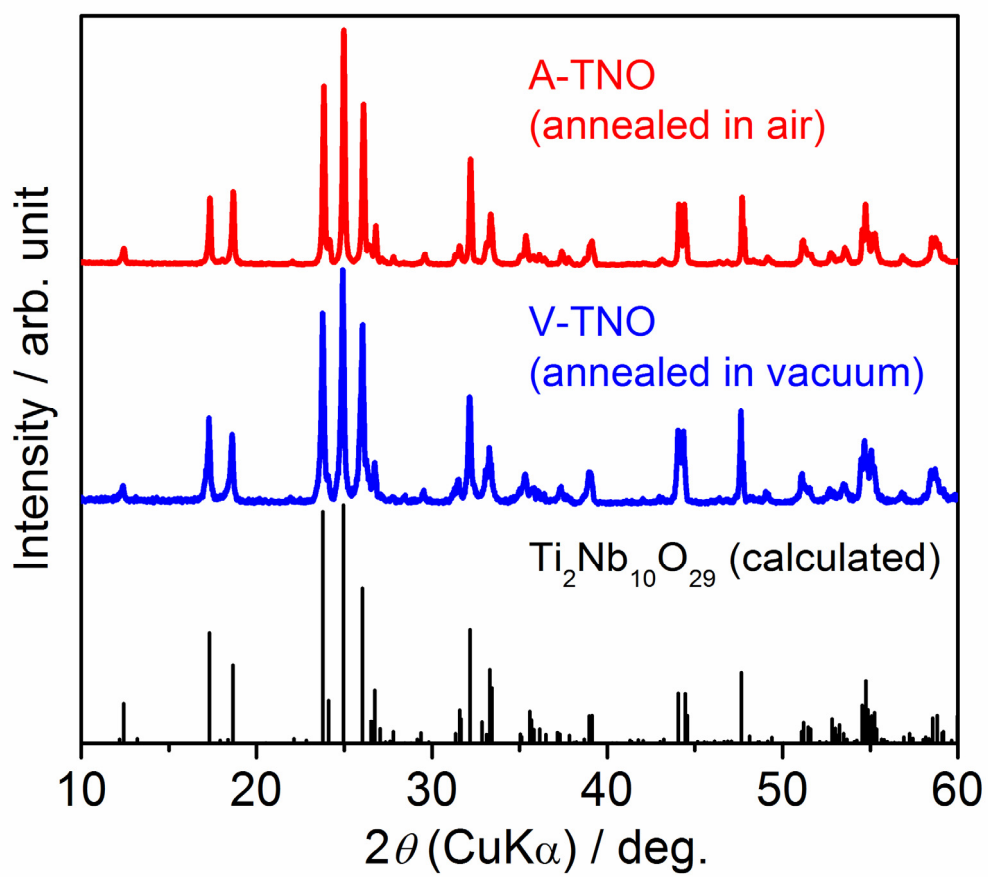


Fig. 1(a)

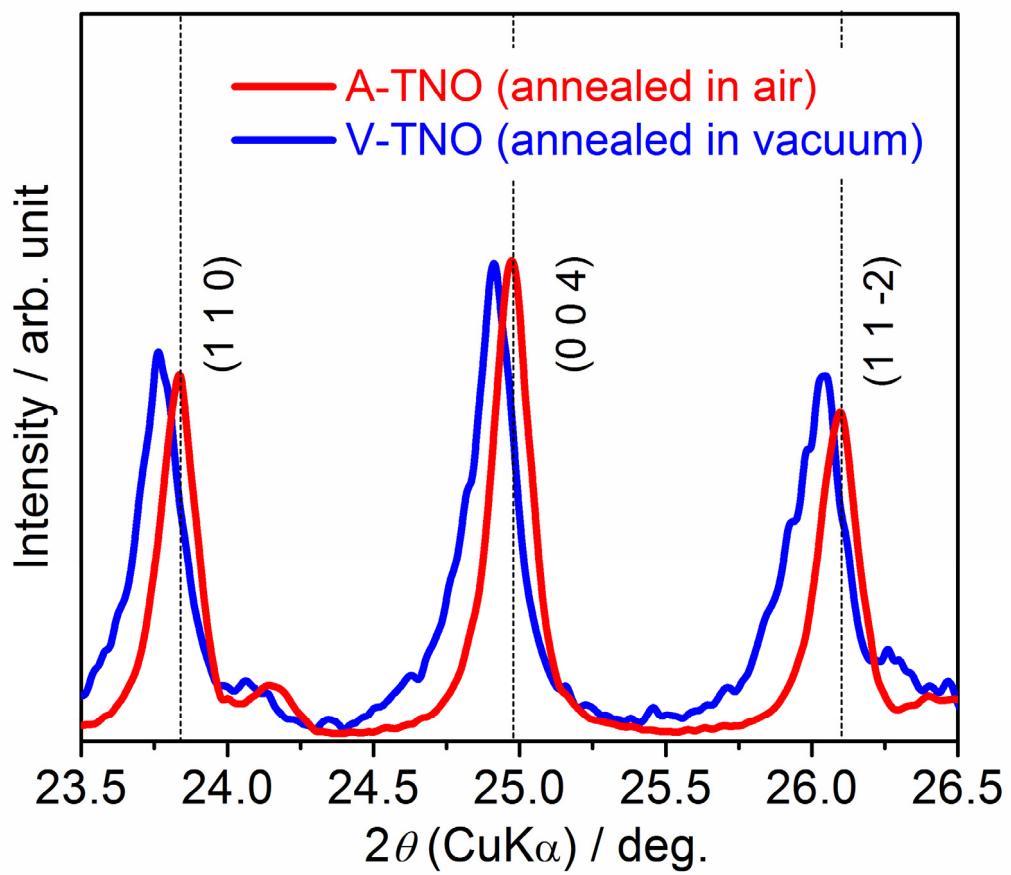


Fig. 1(b)

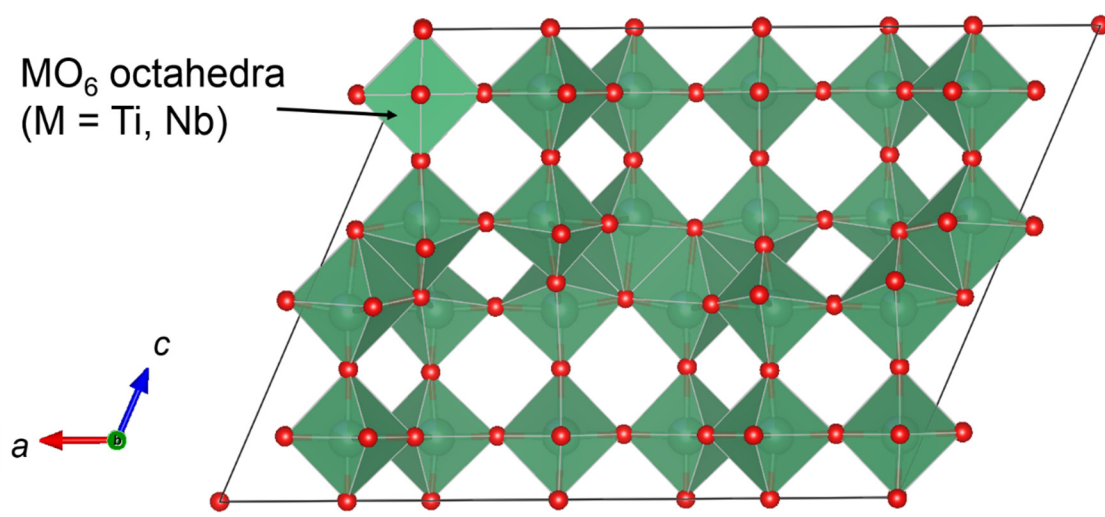


Fig. 1(c)

A-TNO (annealed in air)



Fig. 2(a)



Fig. 2(b)

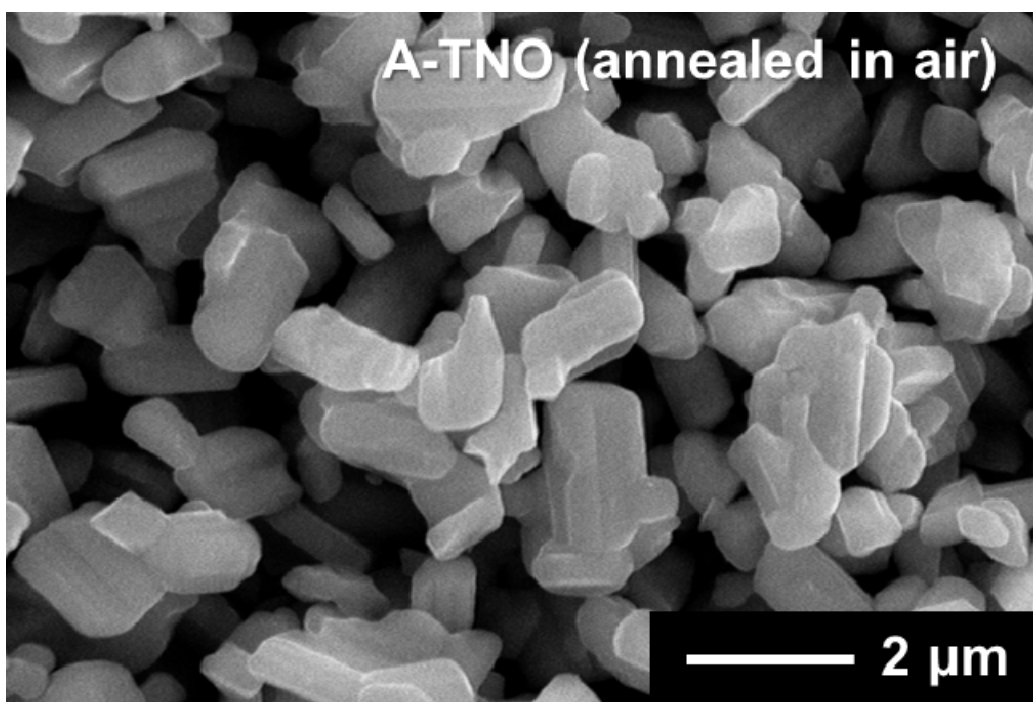


Fig. 3(a)

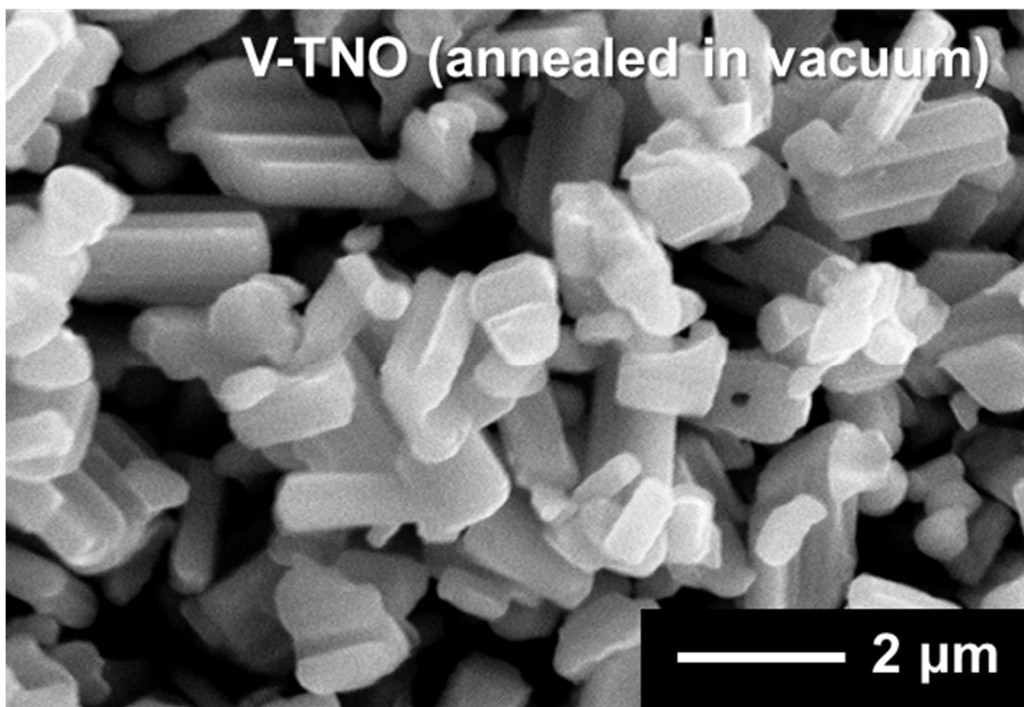


Fig. 3(b)

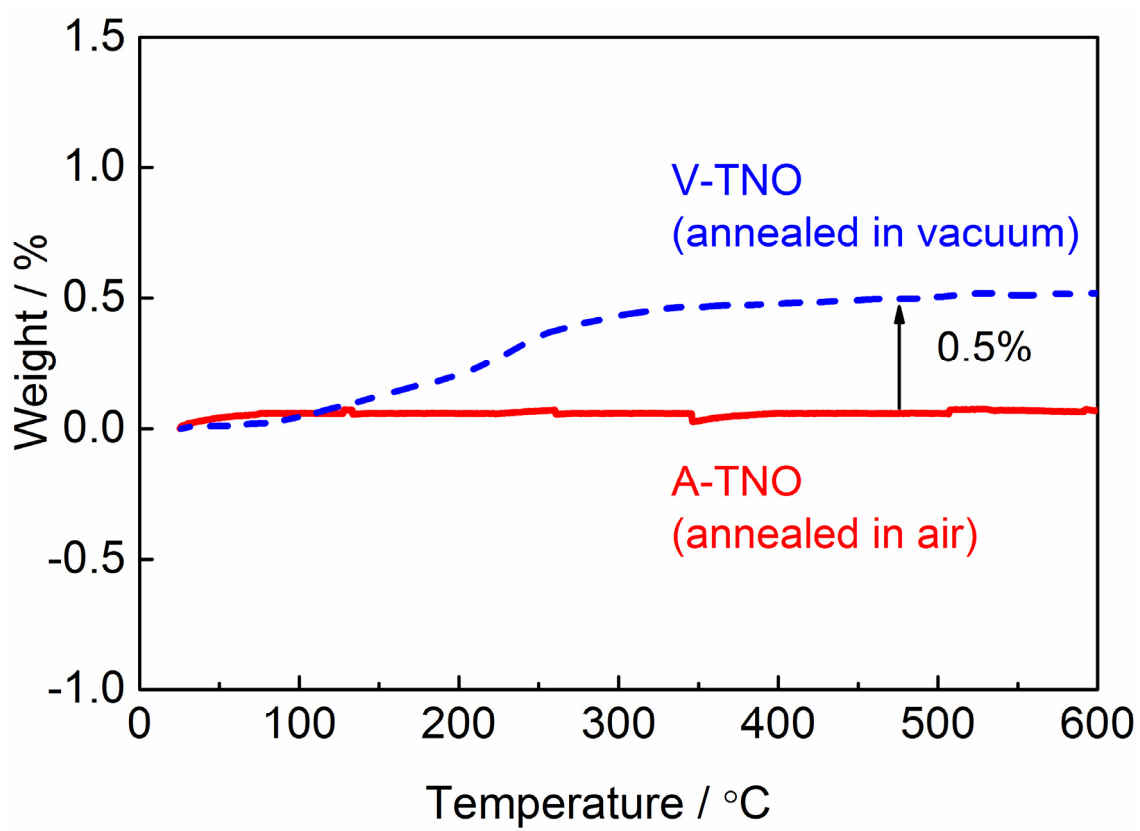


Fig. 4

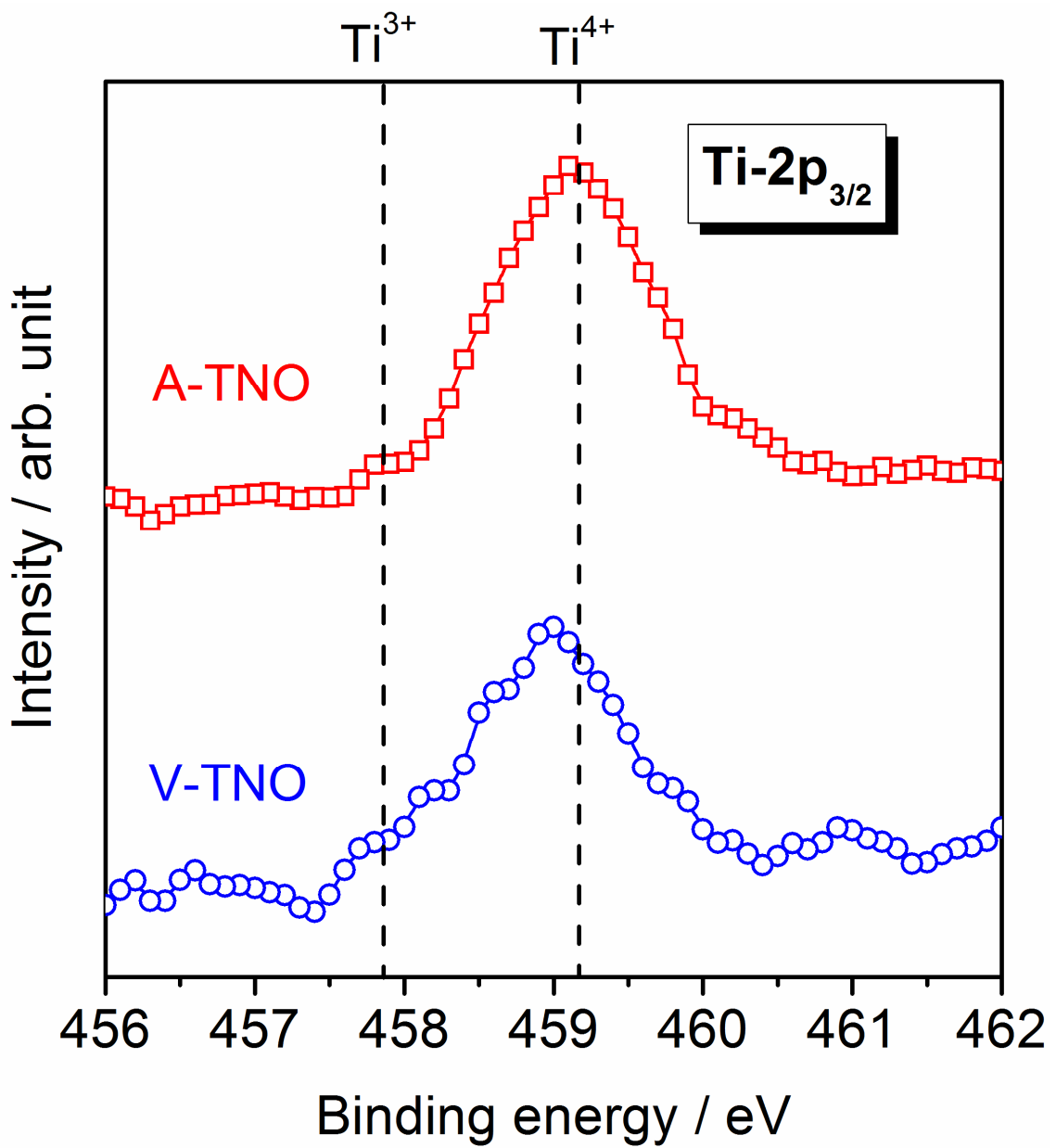


Fig. 5(a)

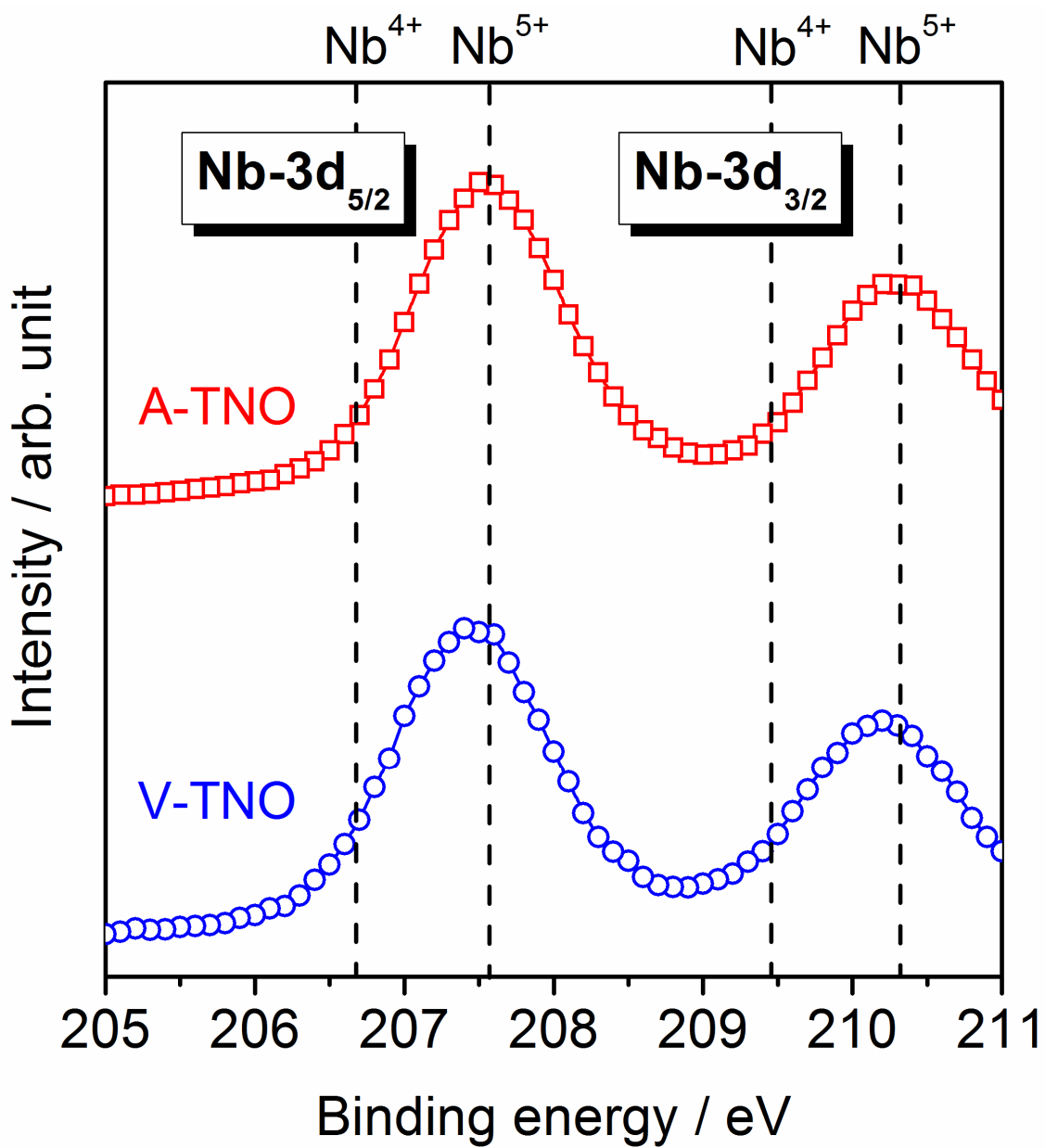


Fig. 5(b)

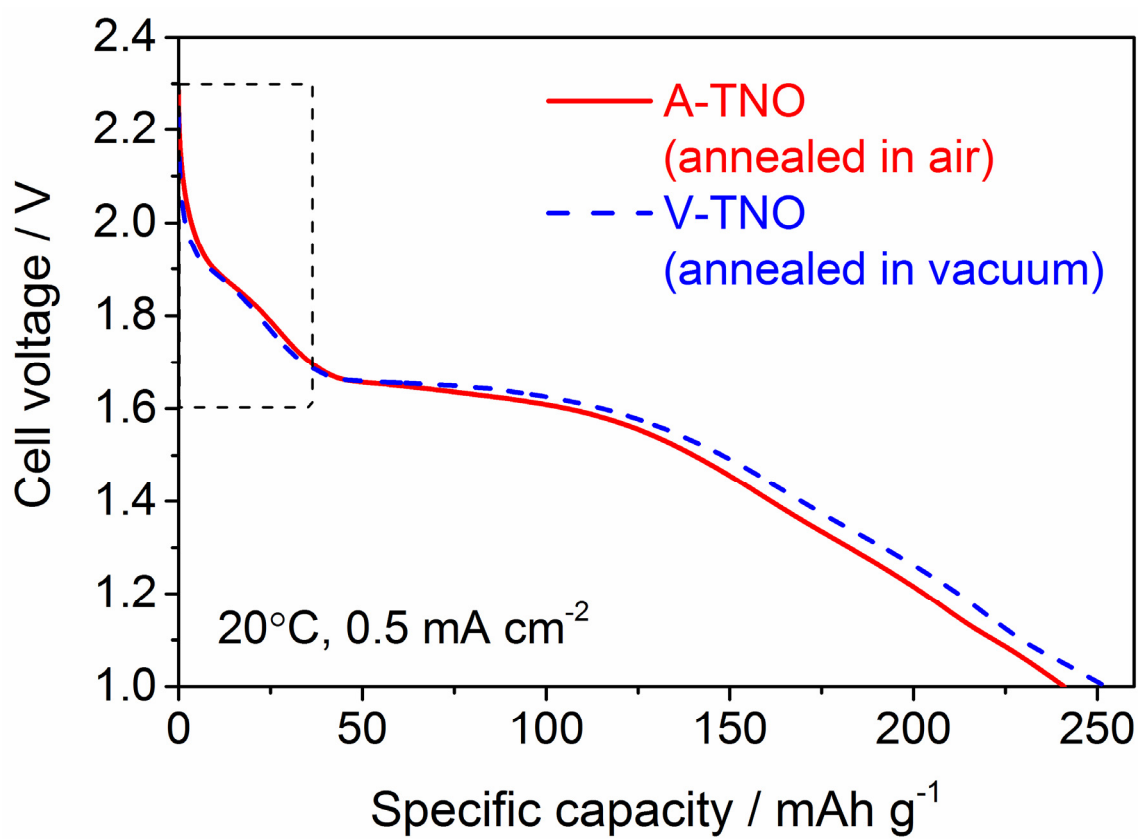


Fig. 6(a)

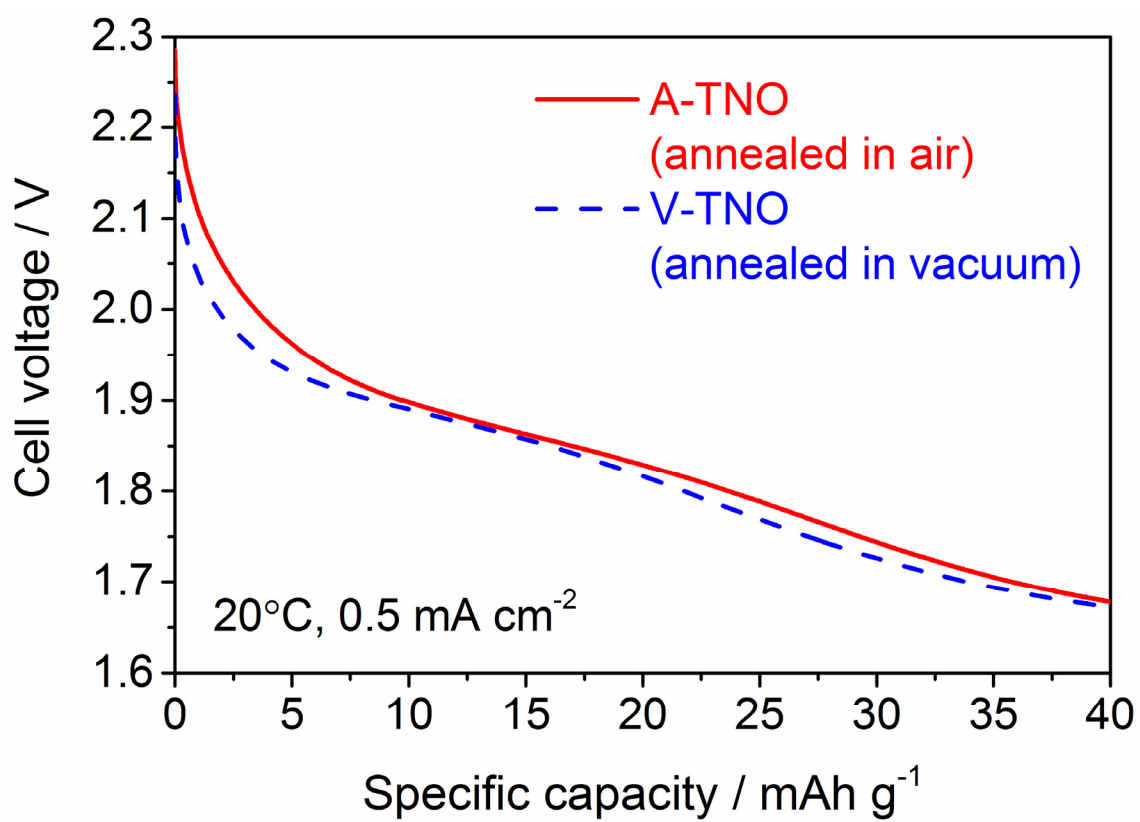


Fig.6(b)

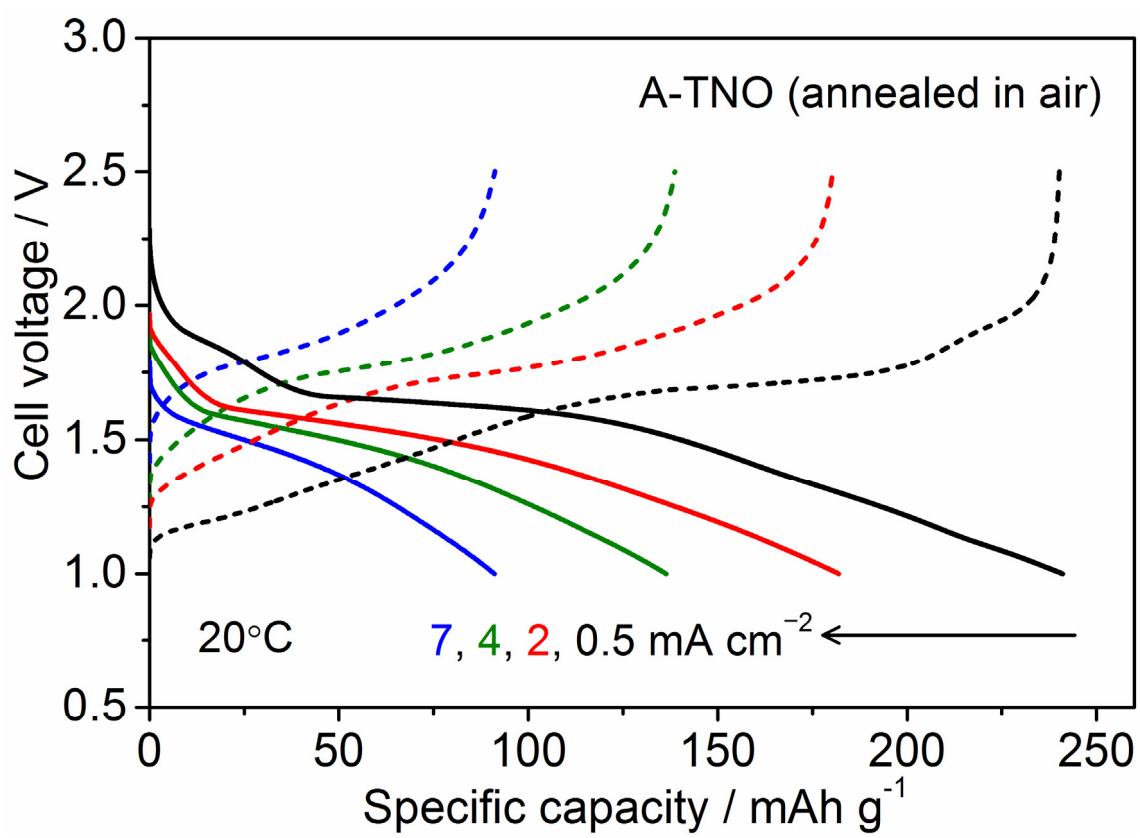


Fig. 7(a)

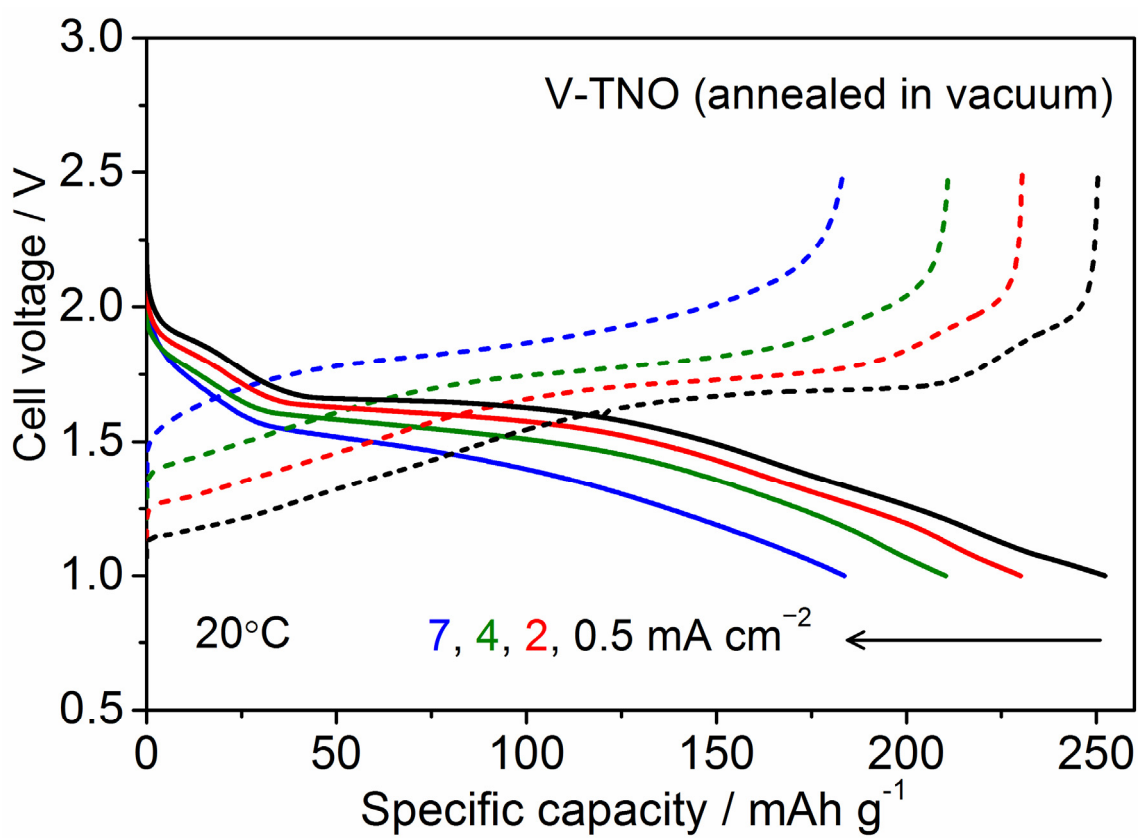


Fig. 7(b)

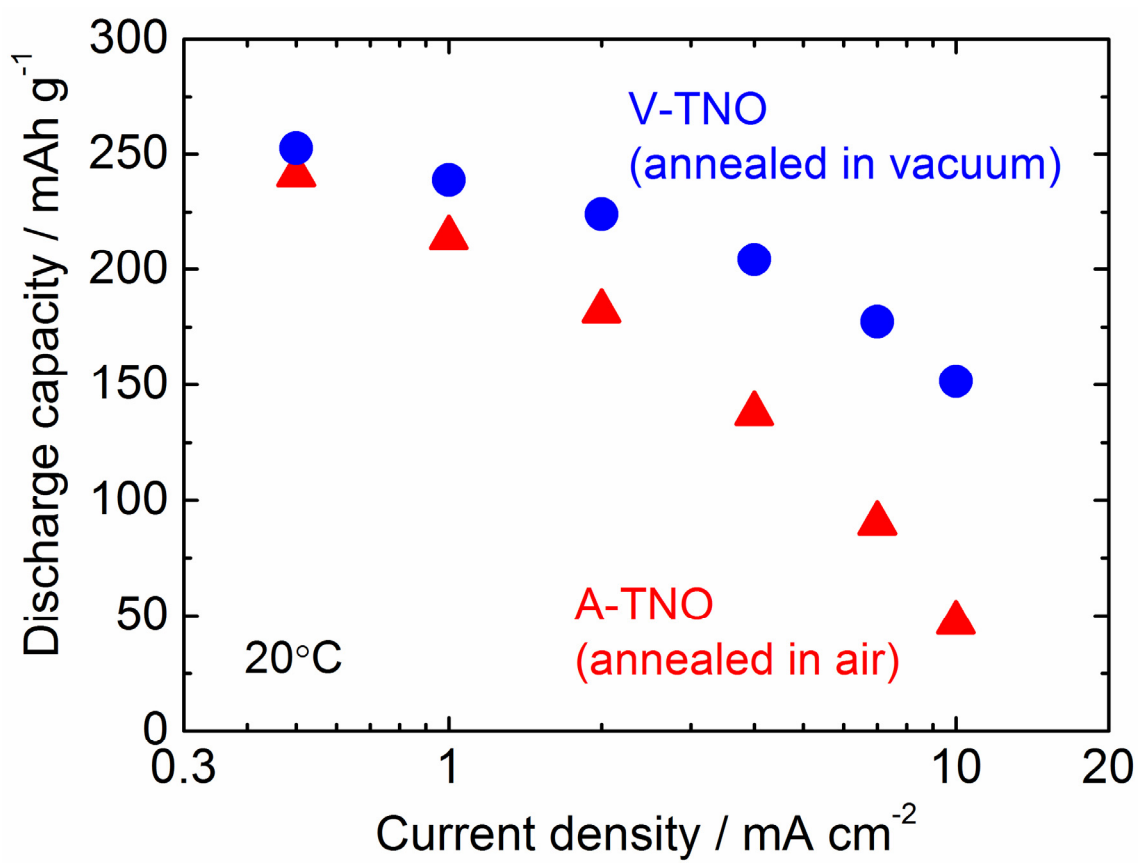


Fig. 8

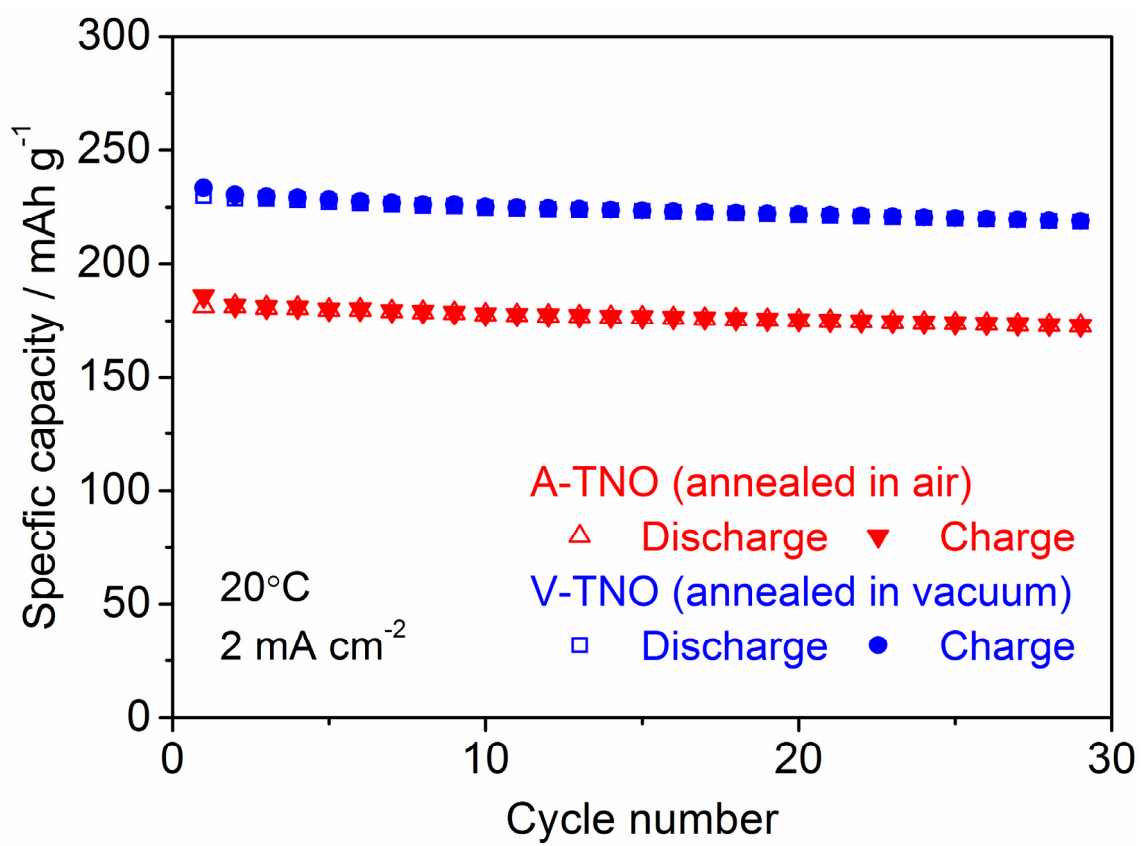


Fig. 9

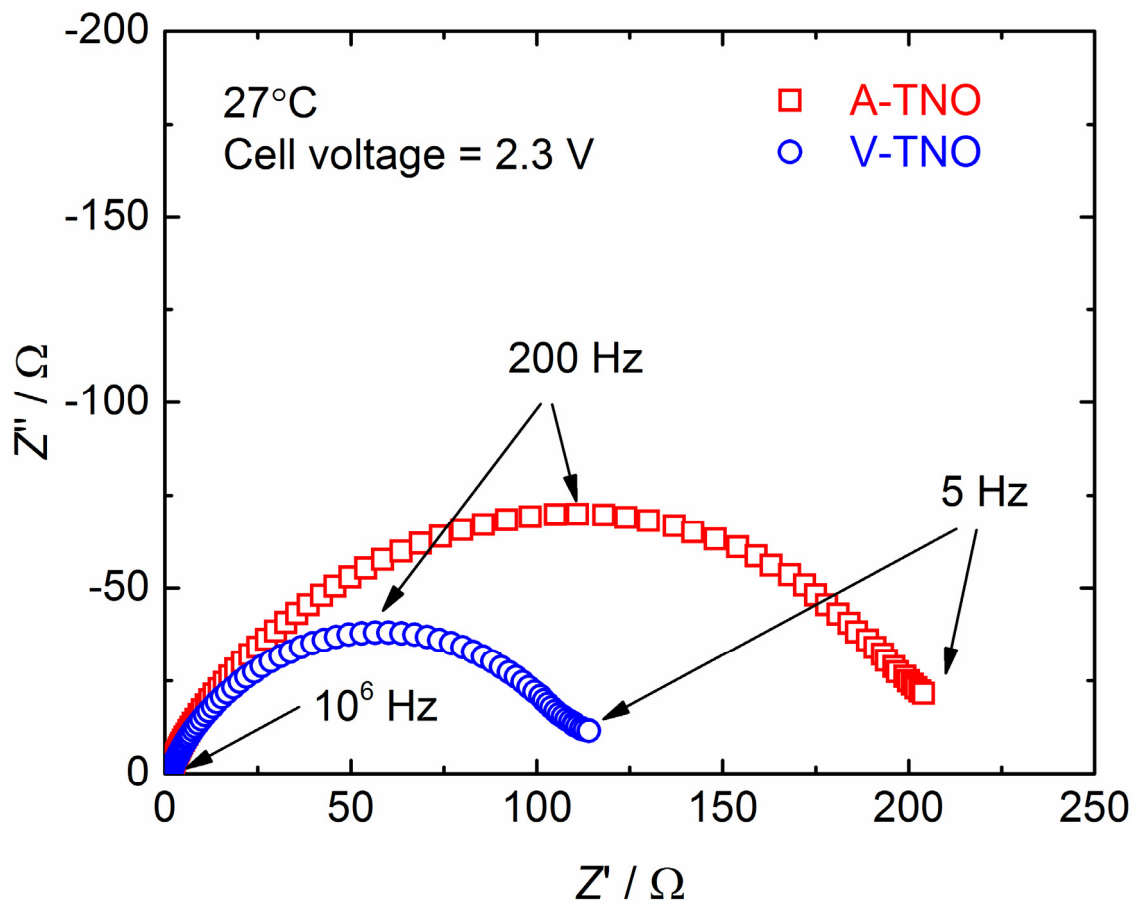


Fig. 10